



# Engineering single Pt Atoms on hybrid amorphous/crystalline CoFe layered double hydroxide accelerates the charge transfer for solar water splitting

Mingze Gao<sup>a</sup>, Nhat Truong Nguyen<sup>b</sup>, Rui-Ting Gao<sup>a,\*</sup>, Xianhu Liu<sup>c</sup>, Xueyuan Zhang<sup>d</sup>, Lei Wang<sup>a,\*</sup>

<sup>a</sup> College of Chemistry and Chemical Engineering, College of Energy Material and Chemistry, Inner Mongolia University, Hohhot 010021, China

<sup>b</sup> Department of Chemical and Materials Engineering, Gina Cody School of Engineering and Computer Science, Concordia University, Montreal, QC H3G 2W1, Canada

<sup>c</sup> Key Laboratory of Materials Processing and Mold, Ministry of Education, Zhengzhou University, Zhengzhou 450002, China

<sup>d</sup> School of Materials Science and Engineering, China University of Petroleum (East China), Qingdao, China

## ARTICLE INFO

### Keywords:

Solar water splitting

BiVO<sub>4</sub>

Single-atom-site Pt

Crystalline-amorphous catalyst

Charge transfer and recombination

## ABSTRACT

Owing to the sluggish kinetics suppressing the oxygen evolution reaction, developing single atoms (SAs) catalyst oxygen evolution reaction catalysts on photoelectrodes is challenging for accelerating charge separation and transfer on photoelectrochemical water splitting. Herein, we elaborately demonstrate the decoration of platinum SAs on hybrid crystalline/amorphous CoFe LDH, and assess the role of SAs on the photogenerated charge carrier separation and transport of photoelectrode. The crystalline/amorphous CoFe LDH is capable of embedding the platinum SAs in its structure by modulating the electronic structure. The single atoms platinum in catalyst enables the effective charge transfer and suppress the charge recombination of the BiVO<sub>4</sub> photoelectrode. The SAs Pt/AC-CoFe catalyst delivers an overpotential of 230 mV at 10 mA cm<sup>-2</sup>, obviously lower than those of AC-CoFe without the introduction of SAs Pt. The SAs Pt/AC-CoFe/BiVO<sub>4</sub> exhibits an excellent PEC performance, a current density of 5.14 mA cm<sup>-1</sup> obtained at 1.23 V<sub>RHE</sub> in 1 M KBI under one sun illumination with a stability of 20 h. This work proposes a rational design of single atoms catalysts decorated on semiconductors and reveals the potential of the single atoms to boost charge carrier kinetics.

## 1. Introduction

With the development of environmental and energy crisis, renewable and clean hydrogen energy has attracted increasing attention in recent years [1–3]. Photoelectrochemical (PEC) water splitting are one of promising strategies for converting solar light into sustainable hydrogen energy [4–6]. Development of semiconductors with sufficient light absorption and efficient charge transfer is important for achieving potential applications. Among various semiconductors [7–11], BiVO<sub>4</sub> can be considered as one of the best candidates due to its suitable bandgap and band edge positions [12,13]. However, the PEC performance of BiVO<sub>4</sub> semiconductor is principally limited, which is far from the theoretical value owing to high charge recombination and sluggish oxygen evolution reaction (OER) kinetics. Moreover, it suffers from serious photocorrosion during long-term operation.

Decoration of various transition-metal-based cocatalysts on the BiVO<sub>4</sub> surface is an efficient strategy to improve photogenerated charge separation and transfer, thereby enhancing the PEC performance and

protecting the semiconductor from photocorrosion [14–17]. Layered double hydroxide (LDH) can act as a popular catalyst for oxygen evolution reaction (OER) on account of its electronic structure, large interlayer distance, and sufficient controllability resulting in low overpotential [18–20]. However, LDH is hampered by its large bulk structure, which is prone to collapse during OER process, and influences OER performance [21–24]. Recently, hybrid structures catalysts, especially the integration of crystalline and amorphous components, show better catalytic performance than the crystalline or amorphous material [25]. Depending on the synergistic advantages of crystalline and amorphous phases, crystalline-amorphous heterostructures provide high electrical conductivity from crystalline phase and a great number of unsaturated coordination sites from amorphous phase with optimized electronic structures, avoiding the unstable character when exposed in corrosive and oxidative environment [26,27]. However, the rational design of hybrid transition-metal cocatalyst for solar water splitting is often ignored. Therefore, it is highly desirable to construct a hybrid crystalline and amorphous LDHs to boost charge carrier transfer and enhance PEC

\* Corresponding authors.

E-mail addresses: [gao-ruiting@qq.com](mailto:gao-ruiting@qq.com) (R.-T. Gao), [wanglei@imu.edu.cn](mailto:wanglei@imu.edu.cn) (L. Wang).

<https://doi.org/10.1016/j.apcatb.2023.122920>

Received 3 April 2023; Received in revised form 20 May 2023; Accepted 25 May 2023

Available online 26 May 2023

0926-3373/© 2023 Elsevier B.V. All rights reserved.

activity and stability of the photoelectrodes.

Single atom catalysts (SAs) have been widely investigated in electrochemistry to maximize the atomic efficiency of noble catalysts and introduce geometric and electronic structures owing to their unique property and capability to accelerate catalytic reaction [28–30]. However, few researches related on SAs are reported in PEC application due to the difficulty of anchor sites on semiconductors. Further on, few reports focus on the determine the roles of SAs to reduce photogenerated charge recombination on PEC devices. In this work, we develop a crystalline/amorphous CoFe LDH heterostructure supported by single atomic Pt (SAs Pt/AC-CoFe) via a facile cation-exchange approach. The hybrid catalyst is further deposited on BiVO<sub>4</sub> photoanodes. The single atoms anchored on AC-CoFe catalyst not only improves its OER process, but also enhances charge separation and transport of the BiVO<sub>4</sub> photoelectrode. The SAs Pt/AC-CoFe catalyst delivers an overpotential of 230 mV at 10 mA cm<sup>-2</sup>, obviously lower than those of AC-CoFe without the introduction of SAs Pt. The resultant SAs Pt/AC-CoFe/BiVO<sub>4</sub> exhibits an excellent PEC performance, a current density of 5.14 mA cm<sup>-1</sup> obtained at 1.23 V<sub>RHE</sub> in 1 M KBI under one sun illumination with a stability of 20 h. Density functional theory calculations demonstrate that SAs Pt/AC-CoFe can optimize the adsorption energies for catalytic intermediates, which facilitate to enhance OER and PEC performances.

## 2. Experimental

### 2.1. Material preparation

**Preparation of ZIF-67, Pt/ZIF-67, AC-CoFe, and SAs Pt/AC-CoFe.** The ZIF-67 was prepared according to the previous report [31]. 1.164 g of Co(NO<sub>3</sub>)<sub>2</sub>·6 H<sub>2</sub>O was dissolved in 200 mL of methanol. Then 1.312 g of 2-methylimidazole was added to the solution. After being stirring for 30 min, the solution was aged for 24 h. Then, the powders were obtained via centrifugation and washing by ethanol for three times. After that, the obtained precipitates were put in a vacuum oven at 60 °C overnight. 50 mg of ZIF-67 was fully dispersed in 10 mL of ethanol, and 250 μL of H<sub>2</sub>PtCl<sub>6</sub> ethanol solution (10 mg mL<sup>-1</sup>) was added to the dispersed solution. After vigorously stirring for 20 h, the obtained powder was collected by centrifugation, washing by ethanol and drying in vacuum at 60 °C overnight to obtain Pt/ZIF-67. 10 mg of Pt/ZIF-67 was dissolved in 10 mL of methanol. 27 mg of FeCl<sub>3</sub>·6H<sub>2</sub>O was dropped into the above methanol solution. After being stirring for 15 min, the mixture and cleaned nickel foam (NF) were put into a 30 mL Teflon autoclave under 120 °C for 2 h reaction. After natural cooling, SAs Pt/AC-CoFe was formed on NF. For the preparation of AC-CoFe, the procedure is same with the synthesis of SAs Pt/AC-CoFe, except that without the induction of Pt source.

**Preparation of BVO, SAs Pt/AC-CoFe/BVO, and AC-CoFe/BVO.** BVO electrode was synthesized by a previously reported method [32]. 100 mL of Bi(NO<sub>3</sub>)<sub>3</sub> solution was prepared by dissolving 4 mmol Bi(NO<sub>3</sub>)<sub>3</sub>·5 H<sub>2</sub>O in 100 mL of 4 mmol KI solution by adding HNO<sub>3</sub> to adjust pH. The solution was mixed with 40 mL of ethanol containing p-benzoquinone. Electrochemical deposition was performed on the fluorine doped tin oxide (FTO) substrate at -0.1 V vs. Ag/AgCl for 180 s to form BiOI film. Then, 0.15 mL of DMSO solution containing 0.03 mmol VO(acac)<sub>2</sub> was placed on the BiOI, and was heated in a muffle furnace at 450 °C for 2 h in air to form the as-prepared BVO. Excess V<sub>2</sub>O<sub>5</sub> on the surface of BVO was removed by soaking electrode in 1 M NaOH for 10 min with stirring. Finally, the BVO samples were rinsed with deionized water and dried in air. The AC-CoFe and SAs Pt/AC-CoFe cocatalysts were decorated on the surface of BVO, following the above procedure, replacing NF with BVO.

### 2.2. Electrochemical and photoelectrochemical measurements

Electrochemical measurements were measured in a standard three-electrode system with an electrochemical analyzer (CHI760D). 1 M KOH was taken as the electrolyte. Current vs. voltage (*I*-*V*) curves were

recorded by scanning the potential from 0 to 0.8 V<sub>Hg/HgO</sub> with a rate of 10 mV s<sup>-1</sup>. The electrochemically active surface areas (ECSA) were measured via cyclic voltammograms (CVs) at various scan rates in a certain potential range. The electrochemical impedance spectroscopy (EIS) was collected with frequency range from 10<sup>-2</sup> to 10<sup>5</sup> Hz.

Photoelectrochemical measurements were measured in a standard three-electrode system with an electrochemical analyzer under simulated sunlight AM 1.5G (100 mW cm<sup>-2</sup>, Beijing Perfectlight Technology Co., Ltd.). All samples were illuminated from the back sides. 1 M KBI were used as the electrolyte. *I*-*V* curves were recorded by scanning the potential from -0.7 to -0.6 V<sub>Ag/AgCl</sub> with a rate of 10 mV s<sup>-1</sup>. The measured potential was converted into a potential with respect to a reversible hydrogen electrode (RHE). Incident photon-to-electron conversion efficiency (IPCE) was measured at 1.23 V<sub>RHE</sub> in 1 M KBI using Xe lamp. Electrochemical impedance spectroscopy (EIS) was performed at 0.8 V<sub>RHE</sub> and a small AC amplitude of 10 mV in the frequency range of 10<sup>-2</sup>-10<sup>5</sup> Hz under AM 1.5G illumination. The surface charge injection efficiency ( $\eta_{\text{surface}}$ ) was measured in 1 M KBI with the addition of 0.2 M Na<sub>2</sub>SO<sub>3</sub>. For the long-term durability, the tested samples were carried out at 0.8 V<sub>RHE</sub> in 1 M KBI.

## 3. Results and discussion

### 3.1. Synthesis of SAs Pt/AC-CoFe catalyst and its OER performance

Fig. 1a shows the illustration of SAs Pt/AC-CoFe heterostructure. Zeolitic imidazolate framework-67 (ZIF-67) was firstly synthesized by a precipitation reaction in a methanol solvent. Scanning electron microscopy (SEM) images of ZIF-67 show uniform particles with rhombic dodecahedral morphology (Fig. 1b-c). ZIF-67 serves as the Co ions source and the shape-directing agent. Pt atoms was then introduced into ZIF-67 in a solution of H<sub>2</sub>PtCl<sub>6</sub> with rigorous stirring, and corresponding sample was noted as Pt/ZIF-67. The modification of Pt causes some wrinkles on the ZIF-67 surface while retaining its metal-organic framework (MOF) structure as observed in Fig. 1d-e. Subsequently, Pt/ZIF-67 can be converted into the single atomic Pt doped amorphous/crystalline (AC) CoFe layered double hydroxide (LDH) through a simple Co and Fe ion exchange by a hydrothermal process in the precursor containing Fe<sup>3+</sup>, and this sample was labelled as SAs Pt/AC-CoFe. SAs Pt/AC-CoFe has a sea urchin-like structure, and its surface is covered with large numbers of fluffy spines (Fig. 1f-g), which can provide a large surface area and more unsaturated sites for OER reaction. We also synthesized the sample of CoFe LDH derived from ZIF-67 without the introduction of Pt atoms (noted as AC-CoFe) for comparison. The morphology of CoFe (Fig. S1) distinguishes from that of SAs Pt/AC-CoFe, where much smooth surface is obtained on the AC-CoFe. This indicates that induced Pt species is vital for modulating amorphous-crystalline structure and exposing more active sites for water reaction.

Transmission electron microscope (TEM) images of SAs Pt/AC-CoFe (Fig. 1h-i) display the irregular burrs of the surface, coincided with its SEM observation (Fig. 1f-g). High-resolution TEM (HRTEM) reveals that the dense crystalline-amorphous heterostructure presents in the LDH structure (Fig. 1j and S2). The lattice spacings of 0.214 nm and 0.260 nm can be indexed to the (107) and (012) planes of FeOOH, respectively. To identify the Pt single atoms dispersed on the SAs Pt/AC-CoFe, high-angle annular dark-field scanning transmission electron microscopy (HAADF-STEM) was employed. Clearly, isolated Pt single atoms as bright spots are distributed on the surface without obvious clusters (Fig. 1k-l and S3), indicating the successful formation of single atom catalyst. Selected area electron diffraction (SAED) pattern proves that SAs Pt/AC-CoFe is composed of both amorphous and crystalline regions (inset of Fig. 1l). The Co, Fe, Pt, and O element mappings imply that a trace of atomic Pt is distributed over the entire SAs Pt/AC-CoFe (Fig. 1m and S4). The content of Pt species in SAs Pt/AC-CoFe is approximately 0.5 wt% from the inductively coupled plasma-optic emission spectrometry (ICP-OES) analysis (Table S1).

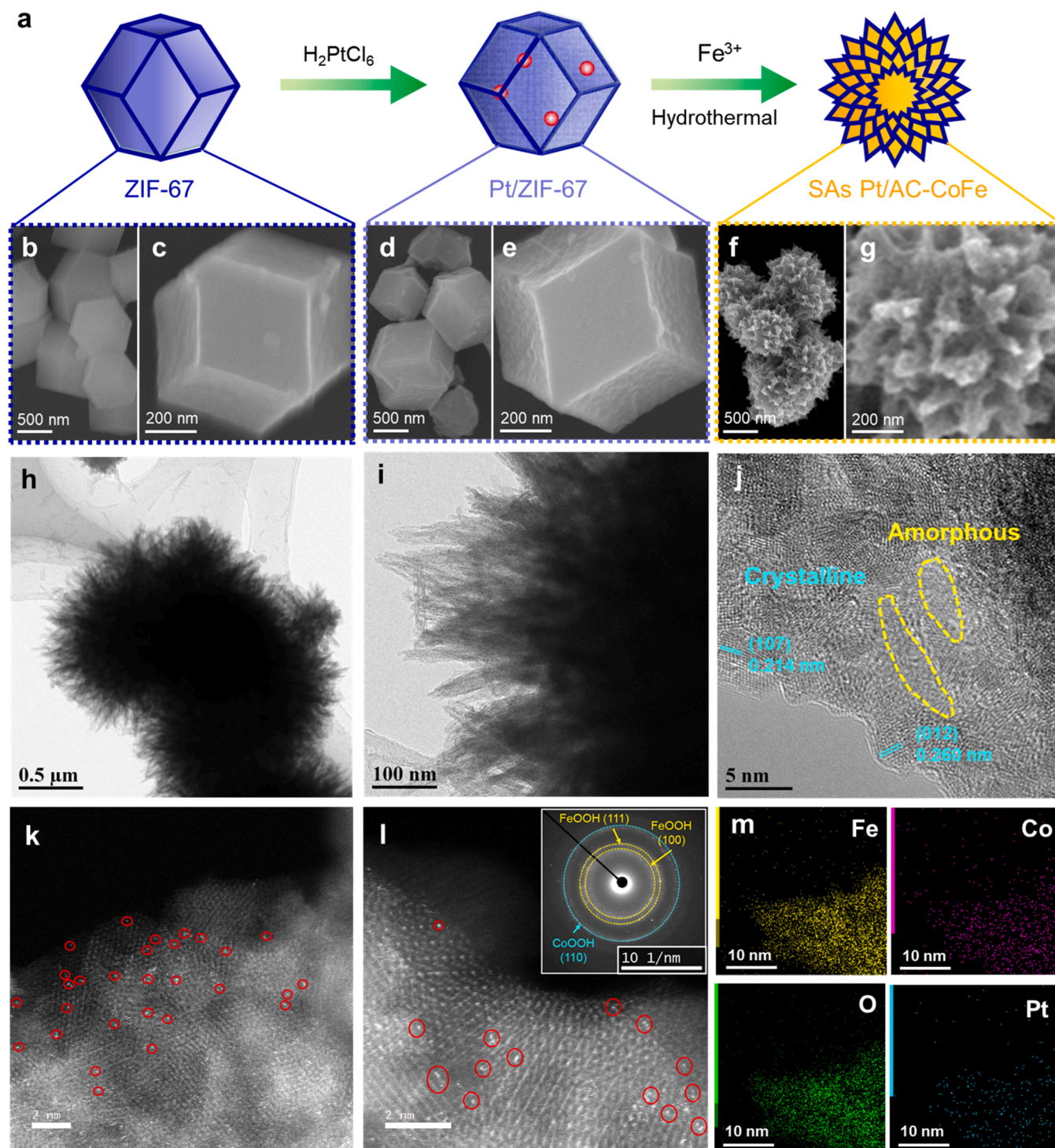


**Fig. 1.** Morphology of SAs Pt/AC-CoFe. (a) Schematic illustration of synthesis of SAs Pt/AC-CoFe; (b-g) SEM images of (b,c) ZIF-67, (d,e) Pt/ZIF-67, and (f,g) SAs Pt/AC-CoFe; (h-j) TEM images, (k,l) HAADF-STEM images and (m) EDS elemental mappings of SAs Pt/AC-CoFe. Inset of l shows the corresponding SAED pattern.

X-ray diffraction (XRD) pattern and X-ray photoelectron spectroscopy (XPS) were performed to explore the phase structure and chemical composition of the electrocatalyst. As shown in Fig. S5, no change in XRD patterns can be observed between ZIF-67 and Pt/ZIF-67. In the case of SAs Pt/AC-CoFe, a poor crystallinity is identified by a broad XRD peak at  $21.1^\circ$ , and the diffraction peak at  $9.2^\circ$  matches with the (003) plane of CoFe LDH (JCPDS 00-006-0075), demonstrating the presence of amorphous-crystalline hybrid structure, corroborated by the disordered crystal lattices from HRTEM image (Fig. 1j). On the XPS analysis of SAs

Pt/AC-CoFe and AC-CoFe, the peaks located at 803.4 eV and 785.0 eV correspond to the  $\text{Co } 2p_{1/2}$  and  $\text{Co } 2p_{3/2}$ , indicating the  $\text{Co}^{3+}$  and  $\text{Co}^{2+}$  oxidation state in samples (Fig. 2a). The Fe 2p XPS spectra of both samples exhibit the typical peaks at 725.5 eV and 712.3 eV (Fig. 2b), assigned to the  $\text{Fe } 2p_{1/2}$  and  $\text{Fe } 2p_{3/2}$  of  $\text{Fe}^{3+}$ . There is a negative shift of binding energy of Fe 2p for the SAs Pt/AC-CoFe in comparison to AC-CoFe, which clarifies the electronic structure change of SAs Pt anchored on AC-CoFe. The Pt 4f XPS spectrum of SAs Pt/AC-CoFe can be marked two peaks at 73.1 eV and 76.2 eV (Fig. 2c), located between



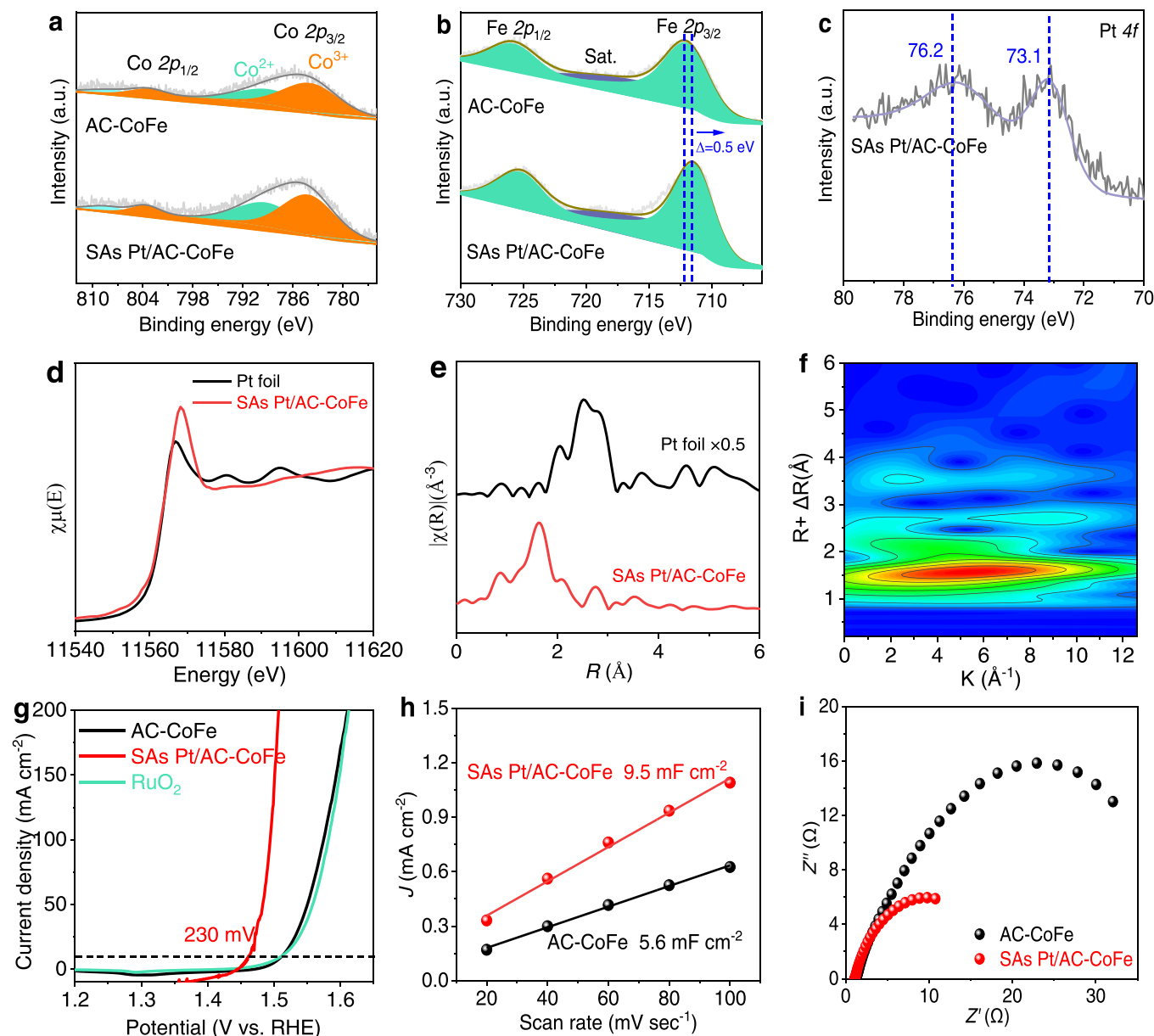


**Fig. 2.** Characterization of SAs Pt/AC-CoFe and OER performance. (a) Co 2p, (b) Fe 2p, and (c) Pt 4f XPS spectra of AC-CoFe and SAs Pt/AC-CoFe; (d) K-edge XANES spectra of SAs Pt/AC-CoFe and Pt foil reference sample; (e)  $k^3$ -weighted Fourier transform Pt  $L_{3}$ -edge EXAFS spectra for SAs Pt/AC-CoFe and Pt foil reference sample; (f) 3D contour WT-EXAFS map with 2D projection of SAs Pt/AC-CoFe; (g) LSV curves of RuO<sub>2</sub>, AC-CoFe, and SAs Pt/AC-CoFe in 1 M KOH; (h)  $C_{dl}$  of AC-CoFe and SAs Pt/AC-CoFe estimated from the plots of the current density vs. scan rate at 1.124 V<sub>RHE</sub>; (i) EIS spectra of AC-CoFe and SAs Pt/AC-CoFe.

metal Pt<sup>0</sup> and PtO<sub>2</sub>, which can be associated with the presence of Pt in sample with a valence state of 0–4 [33]. To further examine the single atom feature, X-ray absorption fine structure (XAFS) spectroscopy was employed to reveal the detailed structure and coordination environment (Fig. 2d and S7 and Table S2). Pt K-edge X-ray absorption near-edge structure (XANES) spectra of the SAs Pt/AC-CoFe and Pt foil indicates the various bonding situation of Pt atoms each other. Fig. 2e–f exhibits the  $k^3$ -weighted Fourier transforms of Pt  $L_{3}$ -edge extended XAFS oscillations of both samples. It can be seen the typical peak at approximately 1.6 Å associated to the Pt–O bond [34], while there is no peak corresponding to a Pt–Pt bond at 2.5 Å in SAs Pt/AC-CoFe. These indicate that the single atom Pt is isolated in the structure, and owing to the amorphous structure, it can facilitate the binding of Pt atoms into its matrix. Moreover, the synergistic electronic interactions among Co, Fe, and Pt cations result in spatial charge redistribution after the introduction of Pt.

The electrocatalytic activities toward OER of AC-CoFe and SAs Pt/

AC-CoFe were performed in 1 M KOH. In Fig. 2g, SAs Pt/AC-CoFe only requires an overpotential of 230 mV to deliver a current density of 10 mA cm<sup>−2</sup>, lower than those of AC-CoFe (281 mV) and the commercial RuO<sub>2</sub> (282 mV). SAs Pt/AC-CoFe displays a Tafel slope of 30 mV dec<sup>−1</sup> (Fig. S8). The electrochemical surface area (ECSAs) was estimated from the electrochemical double-layer capacitance ( $C_{dl}$ ) of the catalytic surface (Fig. S9). Undoubtedly, SAs Pt/AC-CoFe exhibits the higher electrochemical active sites (9.5 mF cm<sup>−2</sup>) compared to the AC-CoFe (5.6 mF cm<sup>−2</sup>) normalized by ECSA (Fig. 2h), implying higher exposed active site in the former. EIS measurements reveal that SAs Pt/AC-CoFe possesses the smaller charge-transfer resistance compared with the AC-CoFe (Fig. 2i), proving the enhanced OER kinetics of SAs Pt/AC-CoFe. The excellent OER reaction kinetics of the SAs Pt/AC-CoFe can be attributed to the amorphous/crystalline hybrid interface and the introduction of Pt SAs, which lowers the reaction barrier and improves the electrochemical performance of the SAs Pt/AC-CoFe.



### 3.2. Synthesis of SAs Pt/AC-CoFe cocatalyst on BiVO<sub>4</sub> photoanode

Benefiting from better OER activity of SAs Pt/AC-CoFe with amorphous/crystalline hybrid structure, we subsequently deposited this as a cocatalyst on the BiVO<sub>4</sub> (BVO) semiconductor. BVO photoanode suffers from the sluggish charge transfer rate and photogenerated charge recombination during solar water splitting. The BVO electrode was prepared on a fluorine-doped tin oxide (FTO) substrate by an electrodeposition method. The SAs Pt/AC-CoFe was decorated on the BVO by a hydrothermal approach since Pt/ZIF-67 was converted into SAs Pt/AC-CoFe. All the diffraction peaks of SAs Pt/AC-CoFe/BVO are indexed to the monoclinic phase of BiVO<sub>4</sub> (JCPDS No. 83-1699), while no evident diffraction peaks are related to the CoFe LDH (Fig. S10). The pristine BVO shows a worm-like porous structure with an average diameter of 200 nm (Fig. 3a). The smooth surface of BVO becomes rough after the decoration of SAs Pt/AC-CoFe (Fig. 3b-d). TEM images present a nanolayer of 8–20 nm coated on the top surface (Fig. 3d). A crystalline and amorphous phase of cocatalyst layer can be clearly seen (Fig. 3e-f), consistent with the above SAs Pt/AC-CoFe electrocatalyst (Fig. 1j). Co, Fe, and Pt elements are examined in EDS mapping of Fig. 3g, indicating the homogeneous distribution of SAs Pt/AC-CoFe cocatalyst deposited on the BVO nanocrystal. XPS measurement further confirms the single

atom Pt incorporated into amorphous/crystalline CoFe hydroxide (Fig. S11).

### 3.3. PEC performance of SAs Pt/AC-CoFe/BVO

The PEC performances of BVO and AC-CoFe/BVO photoanodes without and with the introduction of Pt SAs were carried out in 1 M KBI in a standard three-electrode system under one sun illumination. As shown in Fig. 4a and S12, the optimized SAs Pt/AC-CoFe/BVO delivers a photocurrent density of 5.14 mA cm<sup>-2</sup> at 1.23 V<sub>RHE</sub> with an onset potential of 0.35 V<sub>RHE</sub>, 3.0 and 1.6 times higher than that of BVO (1.70 mA cm<sup>-2</sup>) and AC-CoFe/BVO (3.2 mA cm<sup>-2</sup>). This indicates that the atomically dispersed Pt sites in CoFe can facilitate to enhance the PEC activity of BiVO<sub>4</sub>. The onset potential of SAs Pt/AC-CoFe/BVO is shifted to the negative direction by about 0.2 eV relative to that of BVO photoanode, and it should be mentioned that the onset potential seems to be more positive in comparison to the literature reported. [13] This is possibly due to that the hydrothermal process leads to the derivation of surface structure based on our previous experience. The applied bias photon-to-current efficiency (ABPE) of SAs Pt/AC-CoFe/BVO photoanode is 1.4% at 0.76 V<sub>RHE</sub>, approximately 5 times higher than that of BVO (0.28%), as displayed in Fig. 4c. The stability of SAs

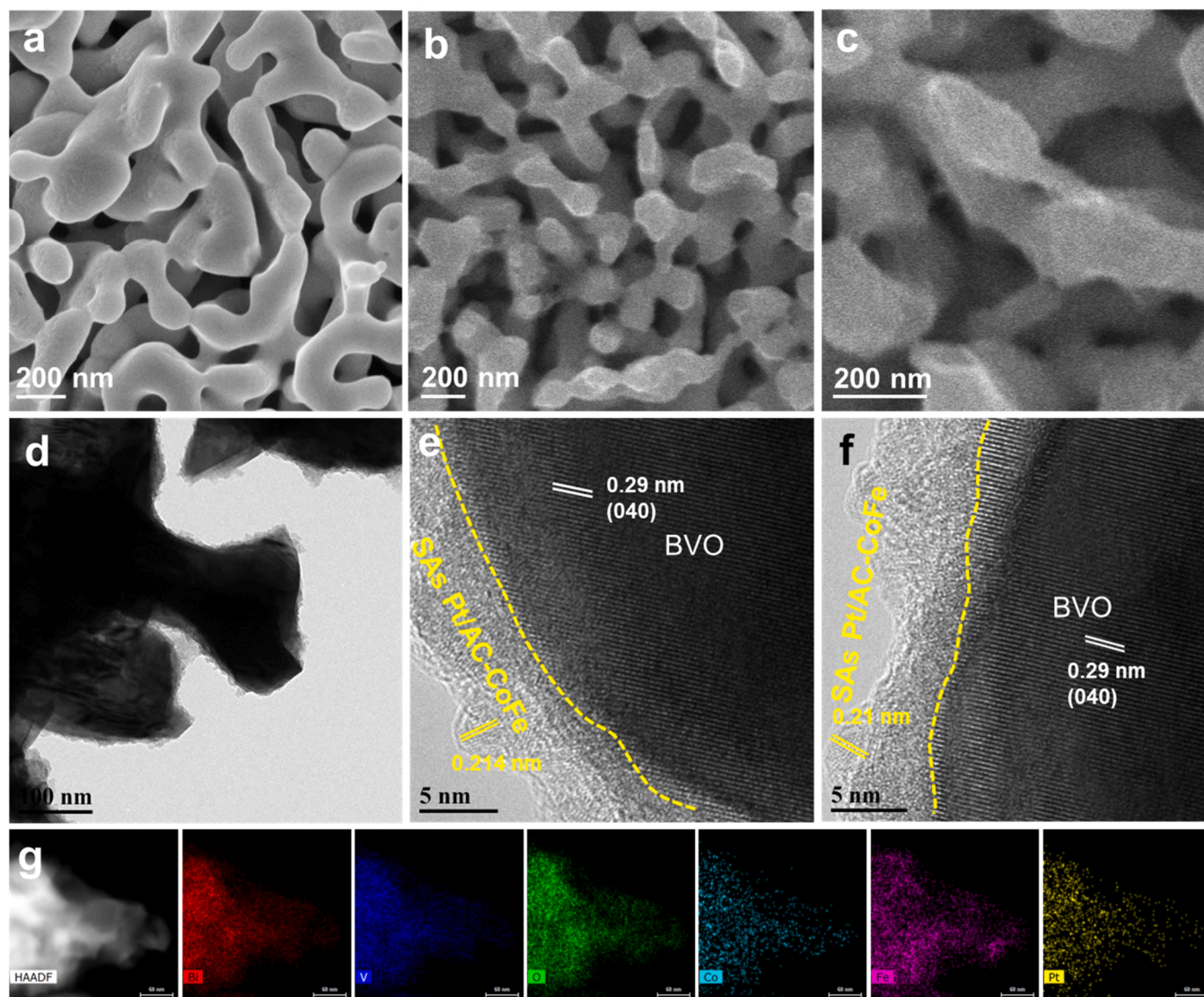


**Fig. 3.** Characterization of SAs Pt/AC-CoFe/BVO. (a-c) SEM images of (a) BVO and (b,c) SAs Pt/AC-CoFe/BVO; (d-f) TEM images and (g) TEM-EDS elemental mappings of SAs Pt/AC-CoFe/BVO.

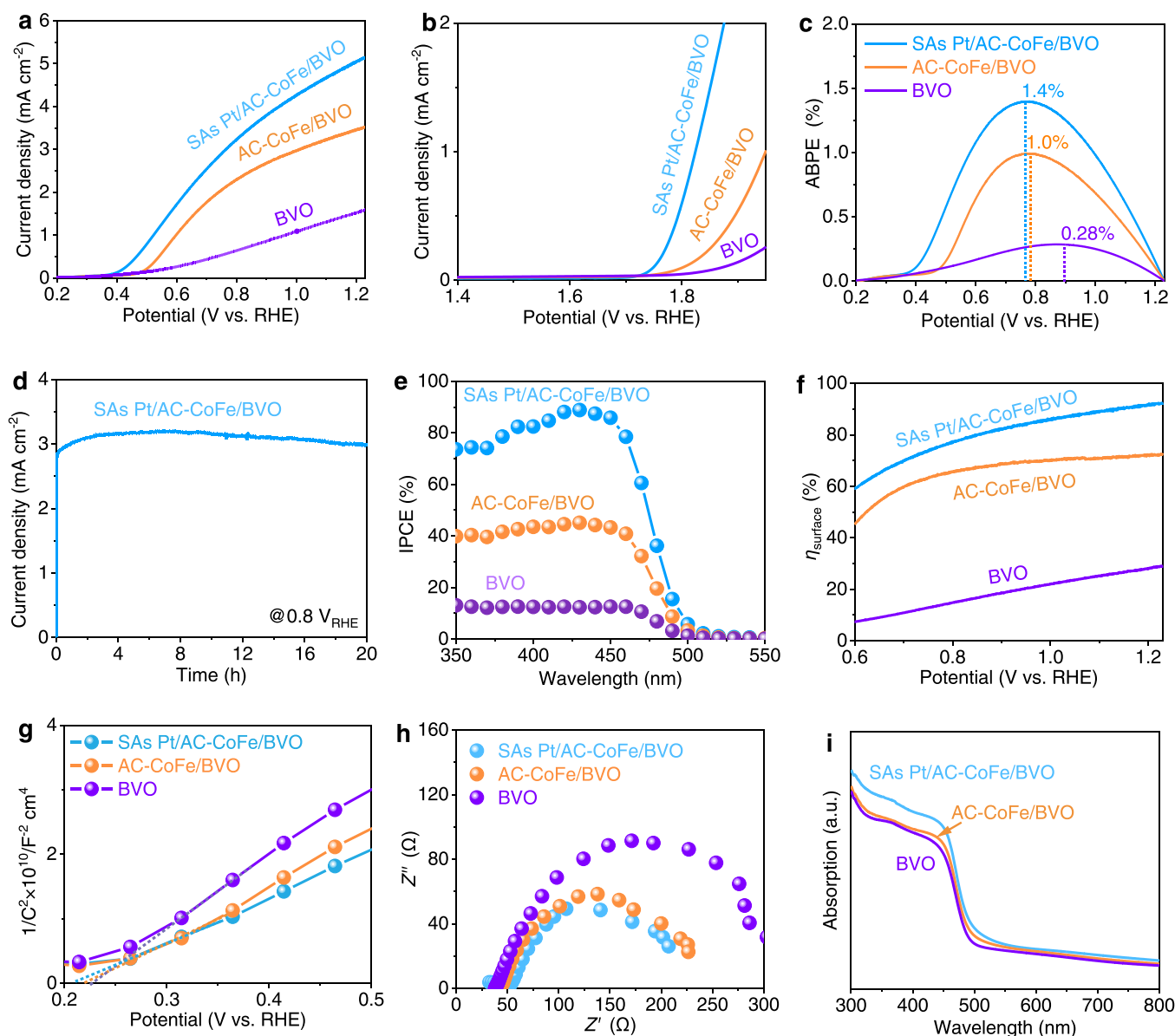


**Fig. 4.** PEC characterization of BVO, AC-CoFe/BVO, and SAs Pt/AC-CoFe/BVO. (a,b) LSV curves (a) under AM 1.5G illumination (100 mW cm<sup>-2</sup>) and (b) in dark in 1 M KBI (pH=9.5); (c) ABPE values; (d) stability measurement in 1 M KBI at 0.8 V<sub>RHE</sub> under AM 1.5G illumination; (e) IPCE values at 1.23 V<sub>RHE</sub>; (f) surface separation efficiencies ( $\eta_{\text{surface}}$ ); (g) Mott-Schottky curves; (h) EIS curves; (i) UV-vis absorption spectra.

Pt/AC-CoFe/BVO was measured, and it shows a stable photocurrent density of 3.0 mA cm<sup>-2</sup> at 0.8 V<sub>RHE</sub> for 20 h (Fig. 4d). MOFs employed as catalysts for water oxidation have received extensive attention cause that it has large specific surface area and abundant exposed oxygen evolution reaction active sites. However, the low conductivity and instability of MOFs restrict their application in the field of photoelectrocatalysis. In this work, adjusting MOFs-derived hydroxides as cocatalyst provides favorable conditions for PEC research, avoiding the restrict of the low conductivity and instability of MOFs.

To better clarify the advantage of SAs Pt/AC-CoFe derived from Pt/ZIF-67, the traditional Pt/CoFe/BVO and CoFe/BVO were synthesized in the similar process without organic species. The photocurrent densities of Pt/CoFe/BVO and CoFe/BVO are obviously lower than that of the SAs Pt/AC-CoFe/BVO (Fig. S13). Meanwhile, the stability test shows that both current densities have an attenuation within 5 h. These results confirm that SAs Pt/AC-CoFe derived from ZIF-67 can effectively protect the photoanode avoiding the photocorrosion owing to the accelerating the charge transfer and water kinetics.

The incident photon-to-current conversion efficiencies (IPCE) of the corresponding photoanodes applied at 1.23 V<sub>RHE</sub> have been examined to demonstrate the influence of monochromatic light upon the photocurrent density. The maximum IPCE value of SAs Pt/AC-CoFe/BVO are approximately 85% at 430 nm (Fig. 4e), which is obviously higher than those of AC-CoFe/BVO and BVO photoanodes. The interfacial charge separation efficiencies are crucial for the surface water oxidation reaction, and we measured the PEC performance in the electrolyte with the addition of Na<sub>2</sub>SO<sub>3</sub> as a hole scavenger (Fig. S14). No doubted that a much higher surface charge separation efficiency was achieved on SAs Pt/AC-CoFe/BVO regarding those of the AC-CoFe/BVO and the pristine BVO (Fig. 4f). The maximum value of  $\eta_{\text{surface}}$  arrives to 92% at 1.23 V<sub>RHE</sub>, demonstrating the contributions of the SAs Pt/AC-CoFe catalyst layer for improving the interfacial charge separation as well as hole transport [35,36].

Mott-Schottky (MS) curves of photoanodes demonstrate that all photoanodes present n-type characteristics on account of the positive slopes (Fig. 4g). Notably, the MS plots indicate that the synergistic effect

of Pt SAC and CoFe LDH improves the charge carrier density as the slope of the SAs Pt/AC-CoFe/BVO decreases, and the intersection with the x-axis is shifted to the negative direction, resulting in the superior charge transfer efficiency of SAs Pt/AC-CoFe/BVO. Fig. 4h shows the electrochemical impedance spectroscopy (EIS) for elucidating the interfacial charge transfer properties. The charge transfer resistance of SAs Pt/AC-CoFe/BVO photoanode is remarkably lower than those of BVO and AC-CoFe/BVO, manifesting the enhanced conductivity and the best charge transfer kinetics of SAs Pt/AC-CoFe/BVO. The optical properties of corresponding photoanodes have been explored by ultraviolet-visible (UV-vis) absorption spectra (Fig. 4i). There is no significant change in light absorption between the pristine BVO and AC-CoFe/BVO, while the light absorption of SAs Pt/AC-CoFe/BVO increases slightly in comparison to the BVO and AC-CoFe/BVO. This reflects in other side that the improved PEC performance of SAs Pt/AC-CoFe/BVO origins from the enhanced light absorption, especially from Pt species with better electron conductivity in cocatalyst layer.

### 3.4. Spectroscopy characterization

To investigate the effect of the charge carrier kinetics on the BVO photoanode, intensity modulated photocurrent spectroscopy (IMPS) was recruited for the corresponding electrodes at various applying potentials. It has been shown that a significant surface state exists when two arcs have been observed in the IMPS spectra, evidencing that tremendous photoexcited carriers accumulated in the surface of the photoelectrode rather than transferred into the electrolyte [37,38]. The carriers accumulated by the surface states could form numerous recombination centers which would deteriorate water splitting reaction. Fig. 5a exhibits the two semicircles in the first and fourth quadrant on the pure BiVO<sub>4</sub> photoanode, indicating the serious recombination happened on the semiconductors [39,40]. In contrast, as AC-CoFe or SAs Pt/AC-CoFe was deposited on the surface of electrodes, there is only one

arc in the fourth quadrant presented in the IMPS spectra (Fig. 5b,c), demonstrating that the photoelectrode charge carriers at the interface of photoelectrode/electrolyte are quickly transferred into the solution to participate in the surface reaction, and the serious recombination can be overcome. Compared to the AC-CoFe/BVO, SAs Pt/AC-CoFe further accelerates the charge carrier transfer and reduces the carrier recombination. This can be also confirmed by the direct observation from chopped light *i*-*t* curves measured at 0.8 V<sub>RHE</sub> (Fig. 5d), in which the ratio of  $i_{\text{initial}}/i_{\text{steady}}$  raises notably for the photoanodes with the decoration of AC-CoFe and SAs Pt/AC-CoFe. The charge diffusion coefficient ( $D_n$ ) can be determined from the frequency at the minimum of the semicircle in the IMPS spectrum:

$$D_n = 2\pi f_{\min} L^2 / 2.35$$

where  $f_{\min}$  is the frequency at the semicircle minimum, and  $L$  is the thickness of photoelectrode. With constant semiconductor thickness,  $D_n$  is only proportional to  $f_{\min}$ , and the results illustrate that the SAs Pt/AC-CoFe is definitely effective to improve the charge transfer of BiVO<sub>4</sub> [39]. Moreover, SAs Pt/AC-CoFe/BVO, AC-CoFe/BVO, and BVO exhibit the defects structure derived from X-band electron paramagnetic resonance (EPR), as displayed in Fig. 5e. Time-resolved photoluminescence (TRPL) spectroscopy was utilized to study the carrier kinetics in semiconductor film (Fig. 5f). The decay curves were measured at 490 nm. All decay curves can be well fitted using a biexponential decay model, and the fitted parameters are summarized in Table S3. With the amorphous/crystalline heterostructure on the BVO surface, both  $\tau_1$  (24.22 ns) and  $\tau_2$  (212.39 ns) become longer compared to the pristine BVO ( $\tau_1 = 20.33$  ns and  $\tau_2 = 142.17$  ns), and  $\tau_1$  and  $\tau_2$  further increase to 29.60 ns and 424.36 ns on SAs Pt/AC-CoFe/BVO, respectively. These above results demonstrate that heterostructure contains a large numbers of oxygen vacancies as OER active sites, and the existence of Pt SAC further provides the active sites in catalyst, eliminating the carrier

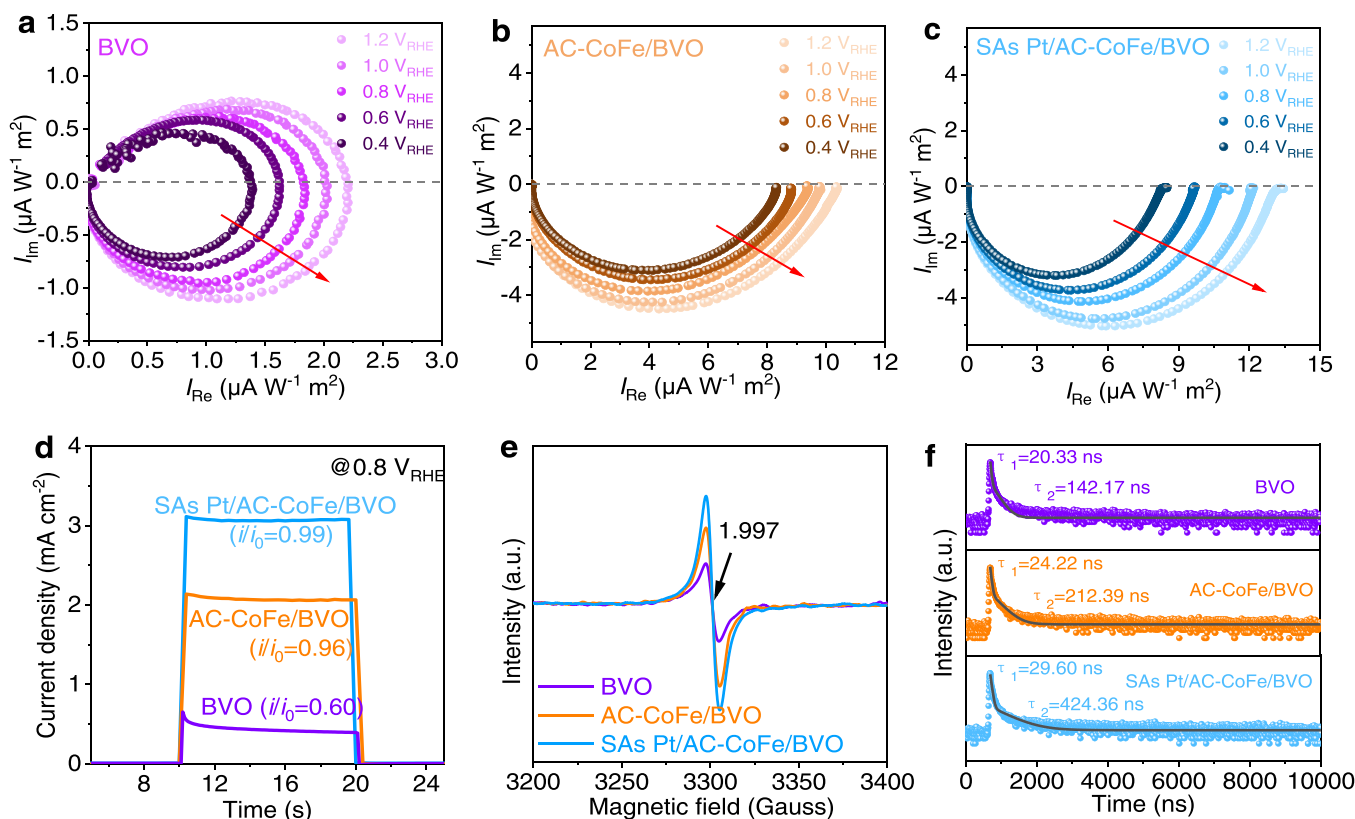


**Fig. 5.** Dynamic kinetics. (a-c) IMPS spectra of (a) BVO, (b) AC-CoFe/BVO, and (c) SAs Pt/AC-CoFe/BVO; (d) chopping light; (e) EPR spectra; and (f) TRPL spectra of BVO, AC-CoFe/BVO, and SAs Pt/AC-CoFe/BVO.



recombination. Moreover, the improved surface state of the photoanode can be attributed to the amorphous and crystalline heterostructure, and Pt SAs suppresses the accumulation of photogenerated charge carriers on the semiconductor surface.

### 3.5. DFT calculations

Computational simulation methods were further implemented to gain a deeper understanding of the role of single atomic Pt. In the model,

as the major component, we adopt crystalline FeOOH as the atomic frame, where edge and terrace surfaces are both modelled as the catalytic surface (because Fe-LDH is a 2d material), while 20% of Fe elements were replaced by the Co elements. A DFT based Metropolis Monte Carlo (MC) simulation was proposed to get the thermodynamic most favorable distribution of the Co atoms. As seen from Fig. S15, Co distributes in both surface and bulk sites, indicating no obvious preference of Co. These lead to the non-Pt structures we used in this work (denoted as CoFe LDH-e/t, 'e' for edge, 't' for terrace). Based on these

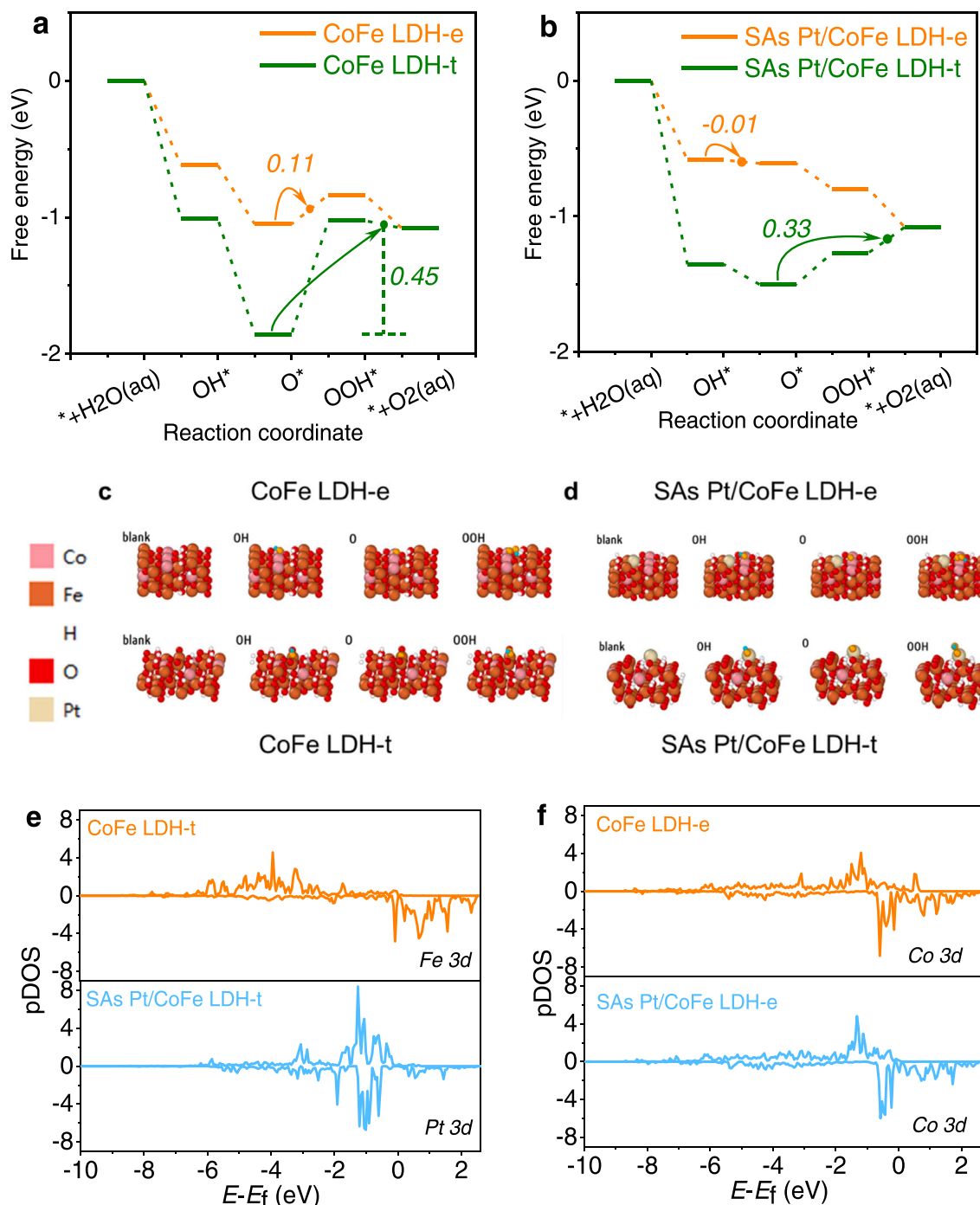


**Fig. 6.** DFT calculations. (a-b) The reaction free energy diagrams of OER on CoFe LDH and SAs Pt/CoFe LDH. The chosen electrode potentials are 1.5  $V_{RHE}$ . The associated TOF determining intermediates (TDI) and virtual TOF determining transition states (TDTS<sup>v</sup>) are marked on the associated paths. All the paths share the same TDI, i.e., the first platform of  $*+H_2O(l)$ . The numbers are the associated  $\delta E^v$  value (unit: eV), which are calculated by energy difference between TDTS<sup>v</sup> and TDI. According to the theory of the “virtual energy energetic span”, the TOF of an electrocatalytic reaction is proportional to  $\exp(-\delta E^v/RT)$ ; (c-d) the associated optimized structures that compose the FED; (e-f) the pDOS of reaction center.

structures, one Pt was introduced in the system to simulate to replace one O atoms, where we chose the thermodynamic most favorable structure. This generates the SAs Pt doped structures used in this work (denoted as SAs Pt/CoFe LDH-e/t). The OER activity is then studied on these structures. At least four possible sites are discussed in each surface to exhaustive search all the possible sites. Computational hydrogen electrode (CHE) method was introduced to discuss the activities [41], while the activity determining term “virtual energetic span” (denoted as  $\delta E^V$ , activity  $\propto e^{-\frac{\delta E^V}{RT}}$ ) proposed by Chen et al. [42] was used to discuss the OER activities. As a result, the associated FED of structures with and without Pt are plotted in Fig. 6a-b. It is evident that structure with SAs Pt performs better by showing much smaller  $\delta E^V$  values (marked by numbers in Fig. 6b). This suggests the atomic Pt can both increases the activities in edge and terrace sites, which helps us to understand the exact role of SAs Pt. Seen from Fig. 6c-d, the active sites are Co for edge sites, while becoming Fe and Pt on terrace sites. This indicates that for edge sites, Pt does not act as the active site, but some auxiliary role; while for terrace sites, Pt itself catalyzes OER. Therefore, we must discuss their characters case by case. For terrace sites, (Fig. 6e-f), the pDOS of Pt is much more symmetrical than that of Fe compare with the Fe sites no-Pt surface, indicating its lower affinity for O species. This is why we see a weaker O binding on SAs Pt/CoFe LDH-t than CoFe LDH-t (On the contrary, we see stronger OOH\* and OH\* adsorption, and this is because the additional hydrogen binding on OH and OOH\* that binds Pt SAs). The weaker O\* binding finally leads to a higher activity. For edge sites, it is found the pDOS of Co are similar, indicating their similar reactivity. Indeed, compared with Fig. 6a and b, we find similar OH\* and OOH\* adsorption, but only a stronger O\* adsorption on SAs Pt/CoFe LDH-e.

#### 4. Conclusions

In conclusion, the CoFe metal oxyhydroxide with SAC Pt synthesized by ZIF-67 has been developed as an effective OER electrocatalyst, which utilizes the large amount of unsaturated active site rich in the A-C heterostructure interface of the catalyst. The site can achieve a low overpotential of 230 mV at 10 mA cm<sup>-2</sup>. The A-C heterostructure interface can also promote the phase change of its own catalyst to optimize OER performance, meanwhile abundant active sites provided by Pt SAC. In addition, the catalyst was wrapped on the surface of BVO semiconductor. Compared with the bare BVO photoanode, the photocurrent density increased from 1.58 to 5.14 mA·cm<sup>-2</sup> at 1.23 V<sub>RHE</sub>. In addition, the stable PEC observed that the water decomposition exceeded 20 h. The excellent PEC performance can be attributed to the vacancy-enriched amorphous-crystallinity heterostructure interface and exposed Pt SAs catalytic active sites generated when SAs Pt/AC CoFe was modified on the BVO photoanode. The new discoveries can also be used other PEC systems for water oxidation reactions.

#### CRedit authorship contribution statement

L.W. supervised the project. M.G. performed the materials synthesis and PEC measurements, and wrote the original manuscript with the instruction of R.-T.G. N.T.N., R.-T.G., X.L., and X.Z. discussed and analyzed the experimental data. R.-T.G. and L.W. revised the manuscript. All authors discussed the results and declared no conflict of interest.

#### Declaration of Competing Interest

The authors declare that they have no known competing financial interests or personal relationships that could have appeared to influence the work reported in this paper.

#### Data Availability

The authors do not have permission to share data.

#### Acknowledgements

The work was supported by the National Key Research and Development Program of China (2022YFA1205200), the National Natural Science Foundations of China (21965024, 22269016), the Inner Mongolia funding (2020JQ01, 21300-5223601).

#### Appendix A. Supporting information

Supplementary data associated with this article can be found in the online version at doi:10.1016/j.apcatb.2023.122920.

#### References

- [1] Y. Jiao, Y. Zheng, M. Jaroniec, S.Z. Qiao, Design of electrocatalysts for oxygen- and hydrogen-involving energy conversion reactions, *Chem. Soc. Rev.* 44 (2015) 2060–2086.
- [2] H. Xu, J. Cao, C. Shan, B. Wang, P. Xi, W. Liu, Y. Tang, MOF-derived hollow CoS decorated with CeOx nanoparticles for boosting oxygen evolution reaction electrocatalysis, *Angew. Chem. Int. Ed.* 57 (2018) 8654–8658.
- [3] I. Ro, J. Qi, S. Lee, M. Xu, X. Yan, Z. Xie, G. Zakem, A. Morales, J.G. Chen, X. Pan, D.G. Vlachos, S. Caratzoulas, P. Christopher, Bifunctional hydroformylation on heterogeneous Rh-WOx pair site catalysts, *PNAS* 609 (2022) 287.
- [4] Y. Xiao, Z. Fan, M. Nakabayashi, Q. Li, L. Zhou, Q. Wang, C. Li, N. Shibata, K. Domen, Y. Li, Decoupling light absorption and carrier transport via heterogeneous doping in Ta<sub>3</sub>N<sub>5</sub> thin film photoanode, *Nat. Commun.* 13 (2022) 7769.
- [5] Y. Zhang, S. Jiang, W. Song, P. Zhou, H. Ji, W. Ma, W. Hao, C. Chen, J. Zhao, Nonmetal P-doped hematite photoanode with enhanced electron mobility and high water oxidation activity, *Energy Environ. Sci.* 8 (2015) 1231.
- [6] H. Zhang, D. Li, W.H. Byun, X. Wang, T.J. Shin, H.Y. Jeong, H. Han, C. Li, J.S. Lee, Gradient tantalum-doped hematite homojunction photoanode improves both photocurrents and turn-on voltage for solar water splitting, *Nat. Commun.* 11 (2020) 4622.
- [7] R.-T. Gao, X. Guo, S. Liu, X. Zhang, X. Liu, Y. Su, L. Wang, Ultrastable and high-performance seawater-based photoelectrolysis system for solar hydrogen generation, *Appl. Catal. B* 304 (2022), 120883.
- [8] Y. Xiao, C. Feng, J. Fu, F. Wang, C. Li, V.F. Kunzelmann, C.-M. Jiang, M. Nakabayashi, N. Shibata, I.D. Sharp, K. Domen, Y. Li, Band structure engineering and defect control of Ta<sub>3</sub>N<sub>5</sub> for efficient photoelectrochemical water oxidation, *Nat. Catal.* 3 (2020) 932–940.
- [9] Z. Zhang, P. Wang, Optimization of photoelectrochemical water splitting performance on hierarchical TiO<sub>2</sub> nanotube arrays, *Energy Environ. Sci.* 5 (2012) 6506–6512.
- [10] W. Li, D. He, S.W. Sheehan, Y. He, J.E. Thorne, X. Yao, G.W. Brudvig, D. Wang, Comparison of heterogenized molecular and heterogeneous oxide catalysts for photoelectrochemical water oxidation, *Energy Environ. Sci.* 9 (2016) 1794–1802.
- [11] Y.-G. Lin, Y.-K. Hsu, Y.-C. Chen, S.-B. Wang, J.T. Miller, L.-C. Chen, K.-H. Chen, Plasmonic Ag@Ag<sub>3</sub>(PO<sub>4</sub>)<sub>1-x</sub> nanoparticle photosensitized ZnO nanorod-array photoanodes for water oxidation, *Energy Environ. Sci.* 5 (2012) 8917–8922.
- [12] R.-T. Gao, N.T. Nguyen, T. Nakajima, J. He, X. Liu, X. Zhang, L. Wang, L. Wu, Dynamic semiconductor-electrolyte interface for sustainable solar water splitting over 600 h under neutral conditions, *Sci. Adv.* 9 (2023) eade4589.
- [13] (a) R.-T. Gao, D. He, L. Wu, K. Hu, X. Liu, Y. Su, L. Wang, Towards long-term photostability of nickel hydroxide/BiVO<sub>4</sub> photoanodes for oxygen evolution catalysts via in situ catalyst tuning, *Angew. Chem. Int. Ed.* 59 (2020) 6213–6218; (b) R.-T. Gao, L. Wang, Stable cocatalyst-free BiVO<sub>4</sub> photoanodes with passivated surface states for photocorrosion inhibition, *Angew. Chem. Int. Ed.* 59 (2020) 6213–6218.
- [14] M. Huang, Z. Huang, H. Zhu, Excellent stability of molecular catalyst/BiVO<sub>4</sub> photoanode in borate buffer solution, *Nano Energy* 70 (2020), 104487.
- [15] F.A.L. Laskowski, M.R. Nellist, J. Qiu, S.W. Boettcher, Metal oxide/(oxy)hydroxide overlayers as hole collectors and oxygen-evolution catalysts on water-splitting photoanodes, *J. Am. Chem. Soc.* 141 (2019) 1394–1405.
- [16] B. He, S. Jia, M. Zhao, Y. Wang, T. Chen, S. Zhao, Z. Li, Z. Lin, Y. Zhao, X. Liu, General and robust photothermal-heating-enabled high-efficiency photoelectrochemical water splitting, *Adv. Mater.* 33 (2021) 2004406.
- [17] Q. Wang, J. He, Y. Shi, S. Zhang, T. Niu, H. She, Y. Bi, Z. Lei, Synthesis of MFe<sub>2</sub>O<sub>4</sub> (M=Ni, Co)/BiVO<sub>4</sub> film for photoelectrochemical hydrogen production activity, *Appl. Catal. B* 214 (2017) 158–167.
- [18] F. Zheng, W. Zhang, X. Zhang, Y. Zhang, W. Chen, Sub-2 nm ultrathin and robust 2D FeNi layered double hydroxide nanosheets packed with 1D FeNi-MOFs for enhanced oxygen evolution electrocatalysis, *Adv. Funct. Mater.* 31 (2021) 2103318.
- [19] L. Lv, Z. Yang, K. Chen, C. Wang, Y. Xiong, 2D layered double hydroxides for oxygen evolution reaction: from fundamental design to application, *Adv. Energy Mater.* 9 (2019) 1803358.

- [20] Z. Chen, M. Ju, M. Sun, L. Jin, R. Cai, Z. Wang, L. Dong, L. Peng, X. Long, B. Huang, S. Yang, T.M. LDH, Meets birnessite: A  $^2\text{D}$ - $^2\text{D}$  hybrid catalyst with long-term stability for water oxidation at industrial operating conditions, *Angew. Chem. Int. Ed.* 60 (2021) 9699–9705.
- [21] P. Zhu, M. Gao, J. Zhang, Z. Wu, R. Wang, Y. Wang, E.R. Wacławik, Z. Zheng, Synergistic interaction between Ru and MgAl-LDH support for efficient hydrogen transfer reduction of carbonyl compounds under visible light, *Appl. Catal. B* 283 (2021), 119640.
- [22] P. Li, X. Duan, Y. Kuang, Y. Li, G. Zhang, W. Liu, X. Sun, Tuning electronic structure of NiFe layered double hydroxides with vanadium doping toward high efficient electrocatalytic water oxidation, *Adv. Energy Mater.* 8 (2018) 1703341.
- [23] L. Zhou, C. Zhang, Y. Zhang, Z. Li, M. Shao, Host modification of layered double hydroxide electrocatalyst to boost the thermodynamic and kinetic activity of oxygen evolution reaction, *Adv. Funct. Mater.* 31 (2021) 2009743.
- [24] W. Chen, B. Wu, Y. Wang, W. Zhou, Y. Li, T. Liu, C. Xie, L. Xu, S. Du, M. Song, D. Wang, Y. Liu, Y. Li, J. Liu, Y. Zou, R. Chen, C. Chen, J. Zheng, Y. Li, J. Chen, S. Wang, Deciphering the alternating synergy between interlayer Pt single-atom and NiFe layered double hydroxide for overall water splitting, *Energy Environ. Sci.* 14 (2021) 6428–6440.
- [25] Y. Zhang, F. Gao, D. Wang, Z. Li, X. Wang, C. Wang, K. Zhang, Y. Du, Amorphous/crystalline heterostructure transition-metal-based catalysts for high-performance water splitting, *Coord. Chem. Rev.* 475 (2023), 214916.
- [26] Z. Gong, R. Liu, H. Gong, G. Ye, J. Liu, J. Dong, J. Liao, M. Yan, J. Liu, K. Huang, L. Xing, J. Liang, Y. He, H. Fei, Constructing a graphene-encapsulated amorphous/crystalline heterophase NiFe alloy by microwave thermal shock for boosting the oxygen evolution reaction, *ACS Catal.* 11 (2021) 12284–12292.
- [27] J. Bak, T.G. Yun, J.-S. An, H.B. Bae, S.-Y. Chung, Comparison of Fe-enhanced oxygen evolution electrocatalysis in amorphous and crystalline nickel oxides to evaluate the structural contribution, *Energy Environ. Sci.* 15 (2022) 610.
- [28] T. Zhang, J. Jin, J. Chen, Y. Fang, X. Han, J. Chen, Y. Li, Y. Wang, J. Liu, L. Wang, Pinpointing the axial ligand effect on platinum single-atom-catalyst towards efficient alkaline hydrogen evolution reaction, *Nat. Commun.* 13 (2022) 6875.
- [29] R. Gao, J. Wang, Z.-F. Huang, R. Zhang, W. Wang, L. Pan, J. Zhang, W. Zhu, X. Zhang, C. Shi, J. Lim, J.-J. Zou, Pt/Fe<sub>2</sub>O<sub>3</sub> with Pt-Fe pair sites as a catalyst for oxygen reduction with ultralow Pt loading, *Nat. Energy* 6 (2021) 614–623.
- [30] Z. Chen, J. Song, R. Zhang, R. Li, Q. Hu, P. Wei, S. Xi, X. Zhou, P.T.T. Nguyen, H. M. Duong, P.S. Lee, X. Zhao, M.J. Koh, N. Yan, K.P. Loh, Addressing the quantitative conversion bottleneck in single-atom catalysis, *Nat. Commun.* 13 (2022) 2807.
- [31] R.R. Kuruppathparambil, T. Jose, R. Babu, G.-Y. Hwang, A.C. Kathalikkattil, D.-W. Kim, D.-W. Park, A room temperature synthesizable and environmental friendly heterogeneous ZIF-67 catalyst for the solvent less and co-catalyst free synthesis of cyclic carbonates, *Appl. Catal. B* 182 (2016) 562–569.
- [32] W. Kim Tae, K.-S. Choi, Nanoporous BiVO<sub>4</sub> photoanodes with dual-layer oxygen evolution catalysts for solar water splitting, *Science* 343 (2014) 990–994.
- [33] Y. Ren, Y. Tang, L. Zhang, X. Liu, L. Li, S. Miao, D. Sheng Su, A. Wang, J. Li, T. Zhang, Unraveling the coordination structure-performance relationship in Pt1/Fe<sub>2</sub>O<sub>3</sub> single-atom catalyst, *Nat. Commun.* 10 (2019) 4500.
- [34] L. Zhang, R. Long, Y. Zhang, D. Duan, Y. Xiong, Y. Zhang, Y. Bi, Direct observation of dynamic bond evolution in single-atom Pt/C<sub>3</sub>N<sub>4</sub> catalysts, *Angew. Chem. Int. Ed.* 59 (2020) 6224–6229.
- [35] W. Feng, M. Bu, S. Kan, X. Gao, A. Guo, H. Liu, L. Deng, W. Chen, Interfacial heterophase construction in nickel/molybdenum selenide hybrids to promote the water splitting performance, *Appl. Mater. Today* 25 (2021), 101175.
- [36] X. Yan, L. Tian, S. Atkins, Y. Liu, J. Murowchick, X. Chen, Converting CoMoO<sub>4</sub> into CoO/MoO<sub>x</sub> for overall water splitting by hydrogenation, *ACS Sustain. Chem. Eng.* 4 (2016) 3743–3749.
- [37] M. Antuch, P. Millet, A. Iwase, A. Kudo, The role of surface states during photocurrent switching: Intensity modulated photocurrent spectroscopy analysis of BiVO<sub>4</sub> photoelectrodes, *Appl. Catal. B* 237 (2018) 401–408.
- [38] Y. Li, K. Wang, D. Huang, L. Li, J. Tao, N.A.A. Ghany, F. Jiang, Cd<sub>x</sub>Zn<sub>1-x</sub>S/Sb<sub>2</sub>Se<sub>3</sub> thin film photocathode for efficient solar water splitting, *Appl. Catal. B* 286 (2021), 119872.
- [39] Y. Lu, Y. Yang, X. Fan, Y. Li, D. Zhou, B. Cai, L. Wang, K. Fan, K. Zhang, Boosting charge transport in BiVO<sub>4</sub> photoanode for solar water oxidation, *Adv. Mater.* 34 (2022) 2108178.
- [40] J.K. Nørskov, J. Rossmeisl, A. Logadottir, L. Lindqvist, J.R. Kitchin, T. Bligaard, H. Jónsson, Origin of the overpotential for oxygen reduction at a fuel-cell cathode, *J. Phys. Chem. B* 108 (2004) 17886–17892.
- [41] J. Chen, Y. Chen, P. Li, Z. Wen, S. Chen, Energetic span as a rate-determining term for electrocatalytic volcanos, *ACS Catal.* 8 (2018) 10590–10598.